

Tailoring Vacancies Far Beyond Intrinsic Levels Changes the Carrier Type and Optical Response in Monolayer MoSe_{2-x} Crystals

Masoud Mahjouri-Samani,^{*,†} Liangbo Liang,[†] Akinola Oyedele,^{†,#} Yong-Sung Kim,^{†,‡,§} Mengkun Tian,^{||} Nicholas Cross,^{||} Kai Wang,[†] Ming-Wei Lin,[†] Abdelaziz Boulesbaa,[†] Christopher M. Rouleau,[†] Alexander A. Puretzky,[†] Kai Xiao,[†] Mina Yoon,[†] Gyula Eres,[⊥] Gerd Duscher,^{||,⊥} Bobby G. Sumpter,[†] and David B. Geohegan[†]

[†]Center for Nanophase Materials Sciences, Oak Ridge National Laboratory, Oak Ridge, Tennessee 37831, United States

[‡]Korea Research Institute of Standards and Science, Daejeon 305-340, Korea

[§]Department of Nano Science, Korea University of Science and Technology, Daejeon 305-350, Korea

^{||}Department of Materials Science and Engineering, University of Tennessee, Knoxville, Tennessee 37996, United States

[⊥]Materials Science and Technology Division, Oak Ridge National Laboratory, Oak Ridge, Tennessee 37831, United States

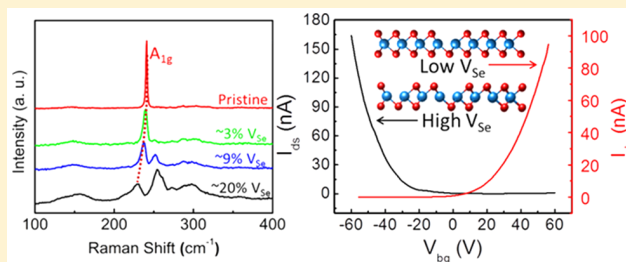
[#]Bredesen Center for Interdisciplinary Research and Graduate Education, University of Tennessee, Knoxville, Tennessee 37996, United States

^ΔComputer Science & Mathematics Division, Oak Ridge National Laboratory, Oak Ridge, Tennessee 37831, United States

Supporting Information

ABSTRACT: Defect engineering has been a critical step in controlling the transport characteristics of electronic devices, and the ability to create, tune, and annihilate defects is essential to enable the range of next-generation devices. Whereas defect formation has been well-demonstrated in three-dimensional semiconductors, similar exploration of the heterogeneity in atomically thin two-dimensional semiconductors and the link between their atomic structures, defects, and properties has not yet been extensively studied. Here, we demonstrate the growth of MoSe_{2-x} single crystals with selenium (Se) vacancies far beyond intrinsic levels, up to ~20%, that exhibit a remarkable transition in electrical transport properties from n- to p-type character with increasing Se vacancy concentration. A new defect-activated phonon band at ~250 cm⁻¹ appears, and the A_{1g} Raman characteristic mode at 240 cm⁻¹ softens toward ~230 cm⁻¹ which serves as a fingerprint of vacancy concentration in the crystals. We show that post-selenization using pulsed laser evaporated Se atoms can repair Se-vacant sites to nearly recover the properties of the pristine crystals. First-principles calculations reveal the underlying mechanisms for the corresponding vacancy-induced electrical and optical transitions.

KEYWORDS: Transitional metal dichalcogenides, vacancies, optical properties, Raman scattering, electrical properties



Two-dimensional metal dichalcogenides (TMDs) have recently been the subject of intense research due to the emergence of extraordinary physical, electrical, and optical properties with decreasing layer thickness and their promise for use in future ultrathin and flexible optoelectronic devices.^{1–5} Compared to exfoliated layers from bulk crystals, “pristine” few-layer TMD crystals synthesized by bottom-up techniques display remarkable heterogeneity, including localized defects such as vacancies,⁶ dislocations,⁷ and substitutional dopants^{8,9} as well as mesoscopic interactions involving misoriented grains,¹⁰ layers,¹¹ substrates,¹² or adsorbates.^{13,14} Such heterogeneity is recognized to result in a wide variability in optoelectronic properties, offering both a control challenge to synthesis and a transformative opportunity for defect engineering.

Defect engineering in 2D-TMDs has been reviewed recently.¹⁵ Both bottom-up^{16,17} and top-down^{18–20} synthesis and processing approaches have been explored to grow nonideal crystals or induce defects and investigate their resultant properties. For instance, electron beam,^{19,21} argon,²⁰ and oxygen²² plasma etching have been used as a top-down approach to process pristine MoS₂ nanosheets and induce defects into their crystalline structures. These types of top-down methods, however, create numerous possible defects including chalcogen vacancies (single or double), metal vacancies, antisite, line, and so forth,^{19–22} which are hard to

Received: June 4, 2016

Revised: July 9, 2016

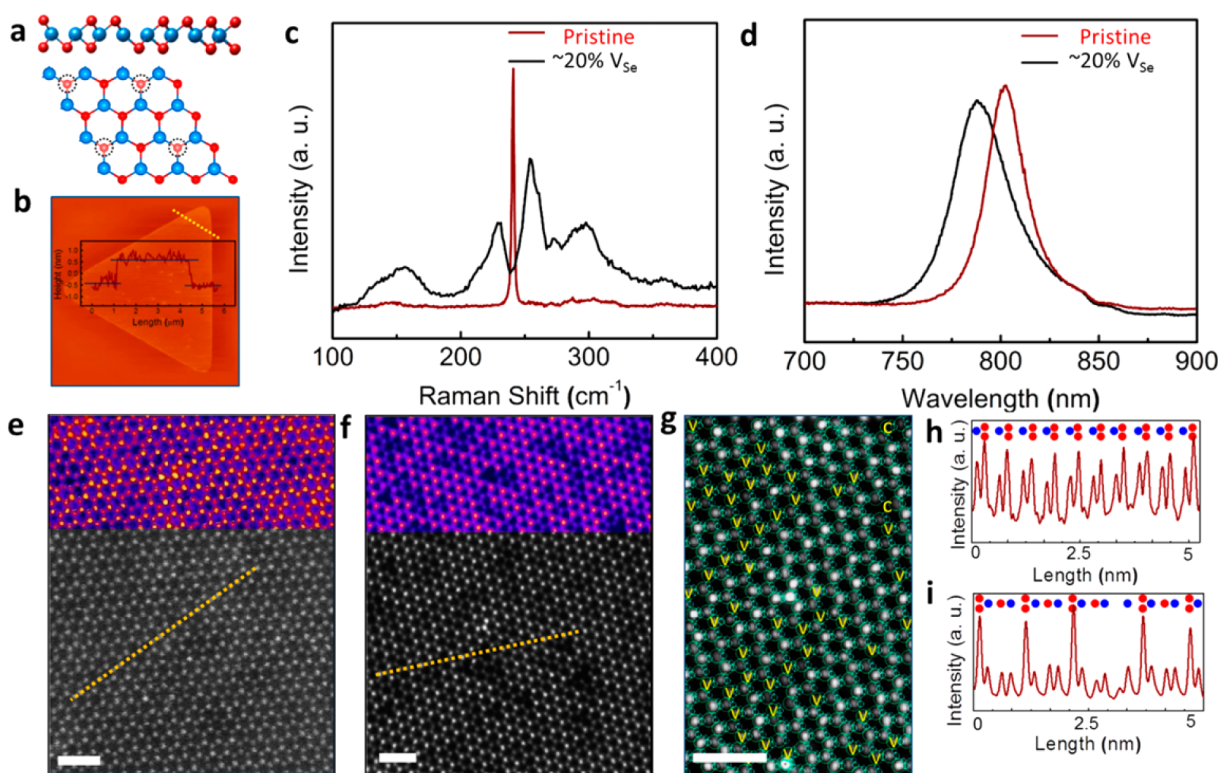


Figure 1. Optical and Z-contrast STEM characterization of Se-deficient crystals. (a) Illustrations showing the side and top view of a Se-deficient MoSe₂ crystal. (b) An AFM image of the crystal showing a thickness of ~ 0.7 nm and a lateral size of ~ 30 μm . (c) Raman spectra of pristine (red) versus Se-deficient (black) crystals that clearly show the absence of the A_g mode at ~ 240 cm⁻¹ and the appearance of two new peaks at ~ 230 and 250 cm⁻¹. (d) PL spectra showing a slight blue shift from ~ 803 nm for pristine (red) to ~ 785 nm for Se-deficient (black) crystals. (e) Atomically resolved Z-contrast STEM image of a MoSe₂ crystal with very low Se vacancy sites (<1%) based upon Z-contrast STEM intensity analysis. (f) Z-STEM image of an as-synthesized and transferred crystal with $\sim 20\%$ Se vacancies. Parts of the images were colored using ImageJ for better visibility. (g) Magnified Z-STEM image of a labeled crystal showing single vacancy positions (yellow “V”) and dual Se column vacancies (yellow “C”). (h, i) Corresponding line intensity profiles as marked in e and f, respectively. The scale bars in STEM images are all 1 nm.

control and relate to specific changes in measured mesoscopic properties. For instance, it is reported that the electron energy required to remove a single sulfur atom from a pristine MoS₂ crystal is much higher than that of an already defective location, resulting in an unavoidable formation of holes as soon as the first vacancy is created.¹⁹ Similarly, as a bottom-up approach, molecular beam epitaxy (MBE)²³ and chemical vapor deposition (CVD)^{24,25} have shown to create a minimal level of defects in the form of chalcogen vacancies, point and line defects,¹⁷ inversion domains,^{23,24} and linear mirror-twin-boundaries, decorating the 2D grains.¹⁶ However, experimental studies that can controllably produce tunable levels of specific defects within TMD single crystals to correlate them with their mesoscopic optical spectroscopy and electrical properties have yet to be performed.

Here we report the nonequilibrium, bottom-up synthesis of single crystalline monolayers of two-dimensional MoSe_{2-x} with controllable levels of Se vacancies far beyond intrinsic levels. Increasing vacancy concentration is shown to induce characteristic shifts in the Raman spectra and a remarkable n-type to p-type transition in electrical transport behavior that is understood through first-principles modeling. These 2D single crystals can retain their crystallinity despite extremely high ($\sim 20\%$) levels of vacancies and represent a new type of highly heterogeneous 2D single crystal with optoelectronic properties that can be tuned controllably via vacancy concentration.

To induce and tune the vacancy concentration in the MoSe₂ crystals (Figure 1a), we developed a laser-based synthesis and processing approach in which continuous laser-evaporation of MoSe₂ powder is used to grow crystals with up to 20% vacancy concentration, followed by pulsed laser evaporation of selenium for digital annihilation and repairing of these vacancies. This novel growth system utilizes a CO₂ laser beam for fast heating and evaporation of MoSe₂ powder, while an adjacent button heater is used to heat a substrate for 2D crystal growth. Specifically, the substrate is first heated to a growth temperature of ~ 700 °C, and then a porcelain alumina boat ($5 \times 5 \times 12$ mm) containing the MoSe₂ powder is heated by a CO₂ laser beam (30 W incident power) to evaporate the MoSe₂ powder for crystal growth. As the temperature of the powder increases, selenium evaporates first, leaving Se-deficient precursors behind that are responsible for the growth of Se-deficient crystals. This nonstoichiometric evaporation was confirmed by elemental analysis of material that was deposited onto room-temperature Si/SiO₂ substrates for different growth times and laser powers. During the first 2 min of the laser heating process, the deposited material was found to be pure Se based on energy dispersive X-ray (EDX) analysis. During deposition at our typical substrate temperature (700 °C), however, no deposit is found indicating that at this temperature this pure Se flux does not stick to the substrate. Nucleation and growth of Se-deficient MoSe₂ crystals were found to occur at later times, in agreement with these measurements. In situ diagnostics of the growth

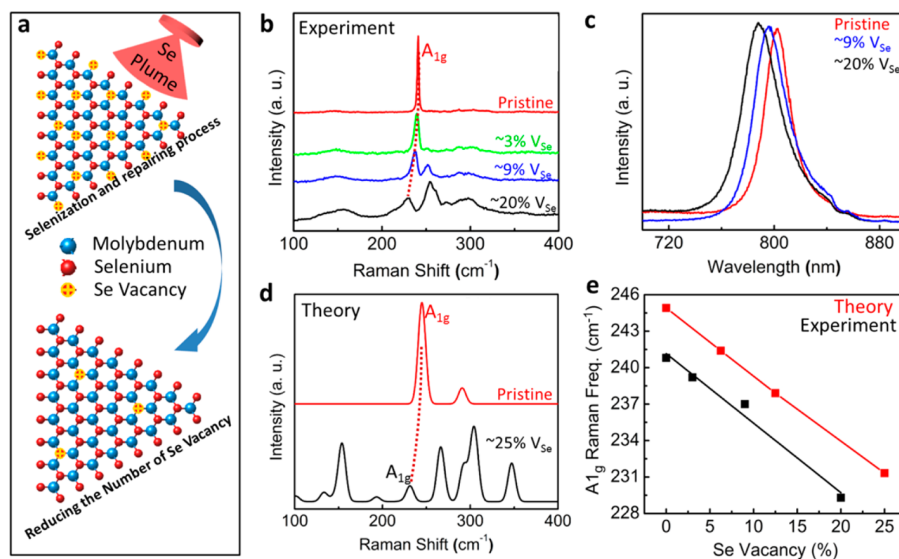


Figure 2. Evolution of optical properties as a function of Se vacancy concentration. (a) Illustration of post selenization and annihilation of vacancies. (b) The A_{1g} Raman peak at 230 cm^{-1} shifted toward the pristine peak at 240 cm^{-1} , and the defect peak at 250 cm^{-1} decreased as the vacancies were annihilated by the post selenization process. (c) PL spectra of the highly defective, partially repaired, and pristine samples. The crystals with higher vacancy concentration show a blue shift in their spectra compared to the pristine samples and partially recover as they are postselenized. (d) Simulated Raman spectra for the pristine system and the one with 25% vacancy concentration. (e) Calculated and experimental vacancy concentration dependence of the signature A_{1g} peak frequency showing a similar trend.

environment during the laser evaporation process will be the subject of a future report.

Moreover, due to lack of sufficient Se atoms floating in the chamber, thermally driven Se losses during the synthesis are not compensated. Regardless of such high level of vacancies, the shape and appearance of the crystals are not affected and still maintain perfect triangular shapes (Figure S1). It should be noted that due to the large number of vacancies, these samples were relatively unstable under ambient conditions, resulting in the degradation of the crystals within a few hours, depending on the Se vacancy concentration. The number of layers and lateral sizes of the as-grown 2D crystals were identified by optical and atomic force microscopy, and as shown in Figure 1b, a typical monolayer MoSe_2 crystal has a triangular shape with a thickness of about 0.7 nm and lateral extent of approximately $30\text{ }\mu\text{m}$.

Optical characterization methods including Raman scattering, absorption, and photoluminescence spectroscopy were utilized to study the optical properties of the Se-deficient MoSe_2 crystals grown directly on SiO_2/Si and quartz substrates.

In the case of pristine MoSe_2 , the most intense and identifiable peak in Raman scattering was the out-of-plane A_{1g} mode located at $\sim 243.7\text{ cm}^{-1}$ for bulk MoSe_2 .^{26–28} The bulk A_{1g} mode tends to shift from $\sim 243.5\text{ cm}^{-1}$ to 240.5 cm^{-1} as the number of layers approaches a monolayer that has been attributed to a decreased interplanar restoring force.^{29,30} However, unlike the pristine monolayer MoSe_2 crystals, the Se-deficient crystals resulted in a large anomaly in characteristic Raman modes. Specifically, the main MoSe_2 Raman mode at $\sim 240.5\text{ cm}^{-1}$ was completely absent, while two new peaks at ~ 230 and 253 cm^{-1} were observed (Figure 1c). Additionally, peaks that were not strong in pristine crystals—i.e., peaks at ~ 150 , 275 , and 350 cm^{-1} —were far more pronounced in the Se-deficient crystals. It appears that due to the large number of Se vacancies, the crystal symmetry of the pristine structure is disturbed, thereby not only damping the pristine main A_{1g}

mode, but also inducing more vibrational modes in the crystal. We also observed a slight blue shift ($\sim 30\text{ meV}$) in the PL spectra of the Se-deficient samples. The PL spectrum of a pristine MoSe_2 grown on a SiO_2/Si substrate is typically located at $\sim 803\text{ nm}$,²⁸ whereas the PL spectra of the Se-deficient samples are blue-shifted by $\sim 15\text{ nm}$ (Figure 1d). The exact mechanism behind this small shift is not clearly understood and could be from different reasons including lattice strain, molecular physisorption,^{31,32} and bandgap renormalization due to defects.

To identify and understand the concentration, distribution, and type (i.e., single side Se vacancy, or double column vacancy) of the vacancies in the crystal structures, various pristine and Se-deficient samples were prepared and studied by atomic resolution Z-contrast STEM, which is capable of identifying individual atoms,³³ or the total mass of atoms within columns, via the image intensity contrast.³⁴ As expected from the pristine MoSe_2 , only a negligible amount of Se-vacancies were observed, and most of the flake was perfect (Figure 1e). However, the Se-deficient samples synthesized in this work (Figure 1f,g) show a large number of (up to 20%) selenium vacancies (labeled “V” and “C”). Note that if a pair of selenium atoms is missing from the top and the bottom of a sheet, hence leaving a hole that is referred to as *column vacancy* in this work (labeled “C” in Figure 1g). Otherwise, they are referred to as *single vacancies* (labeled “V”). The vacancies appeared uniformly distributed across the crystal with a tendency for aggregation where several Se vacancies are found together (Figure 1f,g). The concentration of single vacancies was quantified in each micrograph by counting the total number of columns that were determined to be missing a single Se atom from the Z-contrast STEM images divided by the total number of columns. The quoted vacancy concentration for each growth experiment was obtained by averaging these concentrations from a large set of STEM images. The line

intensity profiles (Figure 1h,i) clearly show the locations and number of atoms in each image as marked.

To further test the effect of vacancies on the optical properties of the material, we performed a post-selenization experiment to systematically annihilate the vacancies. Pulsed laser vaporization of selenium in vacuum was utilized to deliver selenium atoms to the heated crystals in a digital fashion in order to repair the vacancies (Figure 2a). We found that, within a temperature range from 600 to 700 °C, selenization was successful. Above 750 °C, however, the crystals tended to vaporize, and below 600 °C, selenization did not occur. Unlike our sulfurization process reported previously,³⁵ vacancy repair using selenium required a large number of laser-vaporized Se pulses. The vacancy concentration was reduced significantly to ~3% during this process (Figure S2). Figure 2b clearly shows the evolution of Raman modes for different number of laser-generated selenium pulses during the repair process at 600 °C. The black curve shows the spectrum of as-synthesized Se-deficient crystal, while the blue and green curves correspond to the Raman spectra of this crystal after exposure to 500 and 1000 Se pulses, respectively. Note that each spectrum was taken at room temperature after exposure, and the red curve is for a pristine MoSe₂ produced by conventional CVD. As the number of Se pulses increased (thereby reducing the number of Se vacancies), the A_{1g} mode at 230 cm⁻¹ shifted toward that of a pristine MoSe₂ monolayer—i.e., 240 cm⁻¹—and the intensity of the defect related peak at 250 cm⁻¹ decreased. Both the A_{1g}/Si (521 cm⁻¹) and the A_{1g}/(defect peak) Raman peak ratios from each sample presented in Figure 2a decrease as the concentration of the Se vacancy increases (Figure S3). Similarly, the PL (Figure 2c) and absorption spectra (Figure S4) also partially recovered to their pristine state as the crystals were repaired during the post-selenization process.

To understand the new Raman peaks in the defective MoSe₂ monolayers, we carried out first-principles density functional theory (DFT) calculations. Pristine monolayer MoSe₂, belonging to space group *P6m2* (No. 187),³⁶ exhibits a prominent first-order Raman peak around 240 cm⁻¹ with A'₁ symmetry, and a much weaker or nearly nondetectable first-order Raman peak around 287 cm⁻¹ with E' symmetry.^{27,28} When vacancies are introduced into the pristine system, the symmetry is reduced, and the symmetry assignments of the Raman peaks change as well. For simplicity and consistency, the bulk notation of A_{1g} and E_{2g} is used for all systems studied here. According to our atomically resolved TEM images (Figure 1e,g), although *column* vacancies were found, *single* Se vacancies were the most common defect type for monolayer MoSe₂. To model different experimentally accessible vacancy concentrations in monolayer MoSe₂, supercells of different sizes were chosen with a single Se atom or double Se atoms removed in each supercell. We have considered a 4 × 4 supercell (Figure S5) with a single Se atom removed (vacancy concentration 6.25%), a 4 × 4 supercell with two Se atoms removed (vacancy concentration 12.5%), and a 2 × 2 supercell with a single Se vacancy (vacancy concentration 25%). Note that the vacancy concentration is computed as the number of Se vacancy sites divided by the total number of Se atoms in the top Se layer of the supercell. We have also considered pristine monolayer MoSe₂ (vacancy concentration 0%). It should be noted that 25% vacancy concentrations is close to the estimated experimental value before the healing process, 12.5% and 6.25% vacancy concentrations are modeled for the experimental intermediate values during the healing process, and 0% vacancy

concentration is close to the experimental value of the pristine samples.

Figure 2d shows the simulated Raman spectra of the pristine system and the one with 25% vacancy concentration. For the pristine system (red line in Figure 2d), the two first-order Raman peaks, A_{1g} and E_{2g}, discussed above are located at 244.9 and 290.7 cm⁻¹, respectively. The calculated peak positions are in good agreement with the experimental data (~240 and 287 cm⁻¹)^{27,28} with a slight overestimation by ~4–5 cm⁻¹. In addition, the computed E_{2g} peak intensity is indeed much less compared to the A_{1g} peak, which is consistent with the literature^{27,28} in that the E_{2g} peak is much weaker or even nondetectable. Note that in our work, the E_{2g} peak is indistinguishable (red line in Figure 2b), and therefore we focus on the prominent A_{1g} peak for characterization of MoSe₂ monolayers. For the system with 25% vacancy concentration (black line in Figure 2d), our calculations show that the A_{1g} peak is down-shifted to 231.3 cm⁻¹, in good agreement with the experimental Raman spectrum for the most Se deficient sample (black line in Figure 2b). The A_{1g} peak corresponds to out-of-plane vibration of the Se atoms relative to static Mo atoms.^{27,36} Upon the introduction of a Se vacancy into the system, the missing Mo–Se bond leads to an overall reduced restoring force, and consequently the frequency of the A_{1g} peak decreases. Hence, the more Se atoms removed from the system, the weaker the overall restoring force, and consequently a lower A_{1g} peak frequency is expected. We computed two other vacancy concentrations, namely, 6.25% and 12.5%, and found a quasi-linear dependence between the A_{1g} peak frequency and the Se vacancy concentration (Figure 2e). From 0% to 25% vacancy concentration, the frequency decreased monotonically from 244.9 to 231.3 cm⁻¹, consistent with the experimentally observed trend (Figure 2b). Our combined experimental/theoretical results suggest that the characteristic first-order A_{1g} Raman peak can be used as a unique indicator for defect concentration in monolayer MoSe₂, and may be extended to other TMDs systems.³⁷

In addition to the characteristic A_{1g} peak, at 25% vacancy concentration (black line in Figure 2d), the calculations indicate that multiple new peaks appear at ~150, ~270, ~300, and ~350 cm⁻¹, which are likely related to the defects. In the experimental Raman spectrum of the most Se deficient sample (black line in Figure 2b), broad peaks around ~150, ~250, ~270, and ~300 cm⁻¹ also can be observed, and they gradually disappear during the Se healing process, indicating that they are indeed defect-activated peaks. In the case of first-order Raman scattering in a pristine sample, the momentum conservation dictates that only phonons near the Brillouin zone center, Γ , can be involved in the process.³⁸ However, for a defective system, the momentum contribution of a defect can activate phonons with larger wavevectors into the Raman process with the selection rule still satisfied.^{37,39} In monolayer MoSe₂, the first-order A_{1g} Raman peak originates from the A_{1g} phonon at the center of the Brillouin zone (Figure S6). With Se vacancies, nonzone-center phonons can be also involved, and as reported in the literature,^{37,40} the broad peak around ~150 cm⁻¹ is probably from the LA phonon branch at the M point, referred as LA(M) as indicated by blue dash circle (Figure S6). The broad peak around ~300 cm⁻¹ could be assigned to LO(M), and the multiple defect-related peaks between 250 and 300 cm⁻¹ may be ascribed to phonons at other Brillouin zone points.

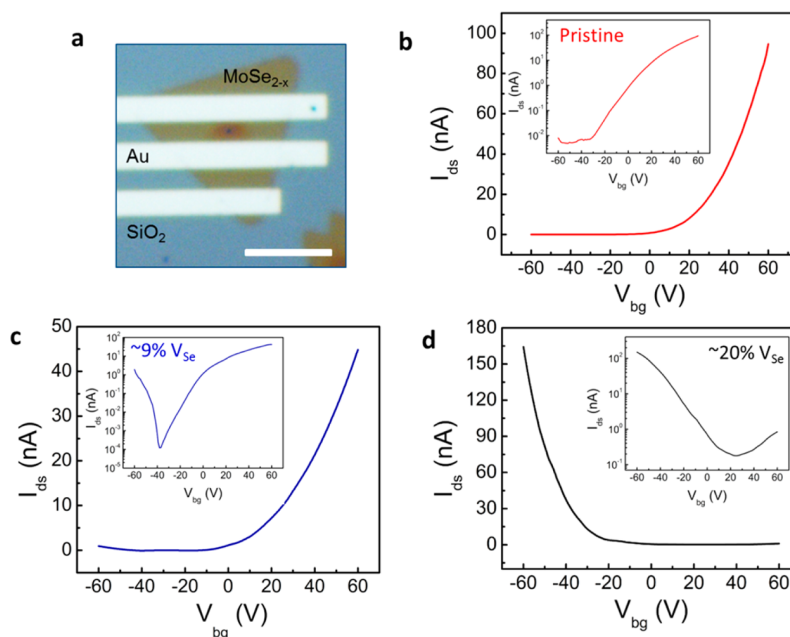


Figure 3. Electrical transport properties transitioning from n- to p-type characteristics. (a) Optical image of a typical device structure. (b) Transport characteristics of a pristine MoSe₂ crystal having Raman characteristics similar to Figure 2b (red curve), showing typical n-type behavior with electron mobility of $\sim 0.05 \text{ cm}^2 \text{ V}^{-1} \text{ s}^{-1}$, and on/off ratio of $\sim 10^5$. (c) Transport characteristics of a MoSe₂ crystal with moderate Se vacancies ($\sim 9\% V_{\text{Se}}$) having Raman characteristics similar to Figure 2b (blue curve), showing a dominant n-type behavior with electron mobility of $\sim 0.021 \text{ cm}^2 \text{ V}^{-1} \text{ s}^{-1}$, and on/off ratio of $\sim 10^5$, but with a slight p-type behavior with hole mobility of $\sim 0.009 \text{ cm}^2 \text{ V}^{-1} \text{ s}^{-1}$. (d) Transport characteristics of a MoSe₂ crystal with a high level of Se vacancies ($\sim 20\% V_{\text{Se}}$) having Raman characteristics similar to Figure 2b (black curve), showing p-type behavior with hole mobility of $0.011 \text{ cm}^2 \text{ V}^{-1} \text{ s}^{-1}$, on/off ratio $\sim 10^3$. The inset in each figure is the same data, only with a logarithmic current axis to clarify the asymmetry.

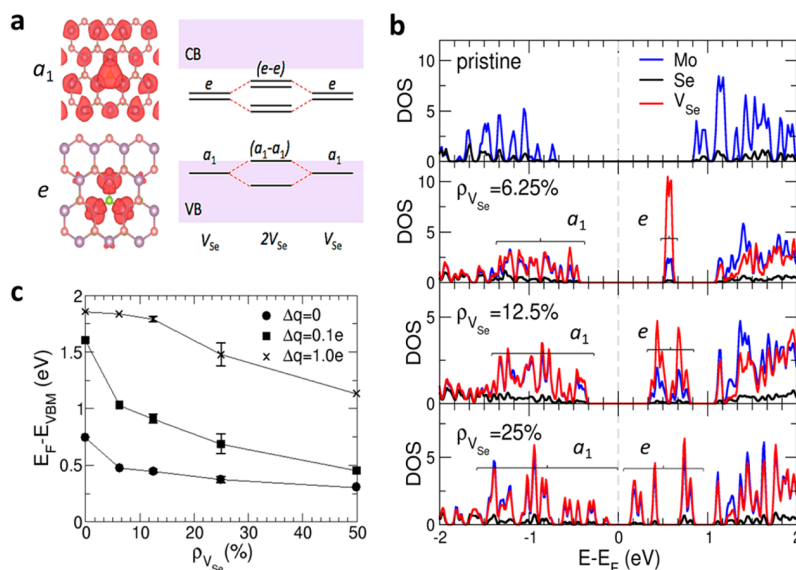


Figure 4. First-principles calculation of electronic transition as a function of Se vacancy concentration. (a) Energy level diagrams of V_{Se} defect states and their hybridization mechanism in monolayer MoSe₂. Charge density plots of the a_1 singlet (isosurface at $\rho = 1.26 \times 10^{-7} \text{ \AA}^{-3}$) and e doublet (isosurface at $\rho = 5.82 \times 10^{-7} \text{ \AA}^{-3}$) states. (b) Local electronic density of states of V_{Se} , Mo, and Se in pristine and Se-deficient material (with various V_{Se} concentrations, $\rho_{V_{\text{Se}}}$). (c) The location of the Fermi level with respect to the VBM with $\rho_{V_{\text{Se}}}$ for the intrinsic ($\Delta q = 0$) and electron doped material ($n = 1.05 \times 10^{14} \text{ cm}^{-2}$ for $\Delta q = 0.1e$ and $n = 1.05 \times 10^{15} \text{ cm}^{-2}$ for $\Delta q = 1.0e$).

The electrical and transport characteristics of monolayer MoSe₂ (both Se-deficient and repaired) nanosheets were also studied. Figure 3a shows an optical image of a typical FET device onto which 5 nm Ti and then 30 nm Au metal contacts were patterned using e-beam lithography and e-beam deposition. The device uses a back-gate configuration with a

250 nm SiO₂ layer serving as the gate oxide and two metal contacts serving as drain and source electrodes. To compare the effect of the vacancies on their transport properties, different devices including pristine and Se-deficient crystals were fabricated and studied. Figure 3b shows the electrical transport properties of a pristine MoSe₂ crystal with n-type behavior

which is consistent with previous reports.^{26,41,42} However, samples with moderate Se vacancy ($\sim 9\%$ V_{Se}) showing Raman signatures similar to Figure 2b (blue curve) have an asymmetry in the transport curve with a tail in the negative gate bias regime, indicating contributions from hole transport as well (Figure 3c). As the Se vacancy increased to a high level ($\sim 20\%$ V_{Se}) with a Raman signature similar to Figure 2b (black curve), devices showed p-type behavior (Figure 3d). The corresponding $I_{\text{d}}-V_{\text{ds}}$ curves are also shown (Figure S7a–c). This remarkable result shows that, by tuning the level of vacancies in MoSe₂ crystals, the MoSe₂ crystals can transition from n- to p-type behavior. Interestingly, the p-type conduction behavior of the highly Se-deficient crystals reverts to n-type behavior after post selenization and repair.

To understand the mechanism behind the transition, further first-principles calculations were performed. Specifically, we investigated the role of Se vacancies (V_{Se}) in the electronic properties of monolayer MoSe₂. We considered various configurations of V_{Se} 's to represent concentrations of 6.25% (one V_{Se} in 4×4 unit cell), 12.5% (two V_{Se} 's in 4×4 unit cell in all the possible configurations), and 25% (two V_{Se} 's in 2×4 unit cell in all the possible configurations). We identified that a selenium vacancy, which has trigonal symmetry, generates three characteristic defect states: a singlet a_1 state inside the valence bands (VBs) of MoSe₂, and doublet e states located deep in the bandgap. The resonant a_1 singlet state hybridizes well with the VB states; extension of the hybridized states is visualized in the charge density plot for the vacancy concentration of 6.25% (Figure 4a). On the other hand, the e gap state is localized near the vacancy site (Figure 4a). As the defect density increases, the distance between the V_{Se} 's becomes closer, resulting in a stronger hybridization between the defect states. The electronic density of states (DOS) reflects well the hybridization mechanism illustrated in the Figure 4a diagram. Figure 4b compares the DOS of MoSe₂ without and with Se vacancies of 6.25, 12.5, and 25%, where the a_1 and e states are highlighted. The degree of hybridization and dispersion of the acceptor states, identified as e , increases with the defect density.

Figure 4c presents the location of the Fermi levels from the VBM, which decreases with the Se-vacancy density ($\rho_{V_{\text{Se}}}$). In pristine monolayer MoSe₂, unintentional n-type doping is typically observed, of which the origin is still controversial, but suggested to be due to the Ti/Au contacts or Re impurities.^{43,44} Since n-type doping is also observed in our experiments, we also consider electron doping (Δq) with 0.1 and 1.0 electrons in the 1×1 supercell of monolayer MoSe₂, corresponding to the charge density of $n = 1.05 \times 10^{14} \text{ cm}^{-2}$ and $1.05 \times 10^{15} \text{ cm}^{-2}$, respectively. As the defect density increases, electrons are trapped by the V_{Se} acceptor states, thereby lowering E_{F} (Figure 4c). Consequently, the band edge of the acceptor-like defect states moves closer to the VBM, which facilitates production of holes in highly Se-deficient structures. Holes are expected in highly defective structures with $\rho_{V_{\text{Se}}} > \sim 10\%$, where a sharp decrease in the Fermi level occurs. Our results also indicate that reduction of E_{F} with increasing V_{Se} concentration is not strongly affected by defect configuration. Note that the Fermi level ranges from 70 to 80 meV for the intrinsic case and 130–280 meV for the electron doped cases, and therefore the n–p transition noted here becomes more difficult in highly doped structures, thereby requiring a higher level of defects to induce the transition.

In conclusion, novel laser-based approaches were introduced for the bottom-up synthesis and top-down healing of nonideal

MoSe₂ monolayer crystals with tunable Se vacancy concentrations up to $\sim 20\%$, far beyond intrinsic values. Atomic-resolution Z-contrast scanning transmission electron microscopy revealed that the great majority of Se vacancies were single atoms lost from either side of the crystal, with far fewer column vacancies where both Se atoms were missing in a column. These vacancies resulted in several notable changes in the electrical and optical properties of the crystals. The characteristic optical signatures of these defects were revealed using Raman spectroscopy and first-principles calculations. With increasing Se vacancy concentration, the A_{1g} mode at 240 cm^{-1} becomes noticeably absent, while two new sharp peaks at ~ 230 and $\sim 250 \text{ cm}^{-1}$ appear. We deduced that the peak at $\sim 230 \text{ cm}^{-1}$ is the defect-induced, red-shifted A_{1g} mode of the system, and the peak at $\sim 250 \text{ cm}^{-1}$ corresponds to a defect-activated phonon band. We showed that upon a post-selenization process using pulsed laser-generated Se atoms, the vacancies were partially repaired, and the original properties of the crystals were partially recovered. Notably, with the decreasing Se vacancy concentration during the repair process, the A_{1g} peak continuously blue-shifts and recovers to the pristine position, suggesting that the characteristic first-order A_{1g} Raman peak can be used as a unique indicator for defect concentration in monolayer MoSe₂, and may be extended to other TMDs systems. Remarkably, both experimentally and theoretically, we observed that the electrical transport properties transitioned from n- to p-type behavior. As the defect density increases, electrons are trapped by the V_{Se} acceptor states, and the E_{F} is reduced. Consequently, the band edge of the acceptor-like defect states moves closer to VBM, which facilitates production of holes in highly Se-deficient structures. Overall, these results reveal a key structure–property link highlighting the transformational opportunity that heterogeneity can play in beyond-ideal 2D materials.

Methods. Device Fabrication and Electrical Measurements. Electron beam lithography (FEI DB-FIB with Raith pattern software) was used for the MoSe₂ device fabrication. First, a layer of PPMA 495 A4 was spin-coated on top of the heterostructure, followed by a $180 \text{ }^\circ\text{C}$ bake on a hot plate. Electrode patterns were designed using L-Edit (layout software) and saved as a gds file for use with the Raith pattern software. After writing the patterns, the device was developed in MIBK1:3 for 70 s and rinsed using isopropanol (IPA). The metal contacts for the device, 5 nm of Ti followed by 30 nm Au, were then deposited using electron beam evaporation. Finally, lift-off was done using acetone/IPA in a sonicator for 20 s.

Electrical Transport Characterization. The electrical measurement of the MoSe_{2-x} field-effect transistor devices was conducted in a vacuum chamber ($\sim 10^{-6}$ Torr) using a Keithley 4200 semiconductor analyzer.

STEM Z-Contrast Imaging and Analysis. All STEM samples were baked at $160 \text{ }^\circ\text{C}$ for 8 h under vacuum before imaging. Scanning transmission electron microscopy (STEM) imaging was performed on an aberration-corrected Nion UltraSTEM-100 operating at 60 kV. The convergence semiangle for the incident probe was 31 mrad. Z-contrast images were gathered for a half angle range of ~ 86 – 200 mrad.

Pulsed Laser Deposition of Selenium. SiO₂/Si source substrates were placed 10 cm from, and parallel to, the selenium target in a cylindrical chamber (50 cm inner diameter, 36 cm tall). The Se target was ablated by imaging at 5:1 reduction a rectangular aperture illuminated by an excimer laser

(KrF 248 nm, 20 ns full width at half-maximum (fwhm)). The resultant spot size and energy density were $2 \times 5 \text{ nm}^2$ and 1 J cm^{-2} , respectively. The target was irradiated at 30° angle of incidence with a repetition rate of 1 Hz at a pressure of 1×10^{-6} Torr.

Optical Characterization of MoSe₂ Crystals. Raman spectroscopy (532 nm excitation source with $\sim 1 \text{ mW}$ of power focused onto the samples through a $100\times 0.9 \text{ NA}$ objective lens) was used to characterize the samples. All PL spectra are plotted without normalization and with the same acquisition time and laser power; however, relative intensities between spectra may differ up to $\sim 5\%$ due to difference in focal spot size.

Density Functional Theory (DFT) Calculations. Plane-wave DFT calculations were performed using the VASP package equipped with the projector augmented-wave (PAW) method for electron–ion interactions.^{45,46} The dynamic matrix was then calculated using the finite difference scheme implemented in the Phonopy software⁴⁷ to obtain phonon frequencies and eigenvectors. Raman intensity calculations were performed for the pristine system and the one with vacancy concentration of 25% (see Supporting Information).

■ ASSOCIATED CONTENT

■ Supporting Information

The Supporting Information is available free of charge on the ACS Publications website at DOI: 10.1021/acs.nanolett.6b02263.

Details of DFT calculations, optical images of MoSe_{2-x} monolayers, STEM image of post-selenized MoSe_{2-x}, Raman peak ratios of MoSe₂ samples with different Se vacancy concentrations, absorption spectra of MoSe_{2-x} monolayers as a function of Se vacancy concentration, atomic structures of monolayer MoSe₂ with different Se vacancy concentrations used in the calculations, phonon dispersion of pristine monolayer MoSe₂, *I*–*V* curves of the MoSe₂ samples with low, moderate, and a high vacancy concentration (PDF)

■ AUTHOR INFORMATION

Corresponding Author

*E-mail: mahjourisamm@ornl.gov.

Author Contributions

M.M.-S. designed and performed the synthesis experiments, and obtained Raman, PL, and absorption data with A.A.P. A.O., M.-W.L., and K.X. participated in the device fabrication and transport characterization. L.L., B.G.S., Y.-S.K., and M.Y. performed theoretical modeling. G.D., N.C., and M.T. carried out the STEM study and analysis. C.M.R., A.A.P., K.W., A.B., G.E., and D.B.G. participated in data analysis, discussions, and manuscript preparation. All of the authors discussed the results and commented on the manuscript.

Funding

Funding is provided by: (1) U.S. Department of Energy, Office of Science, Basic Energy Sciences (BES), Materials Sciences and Engineering Division; (2) U.S. Department of Energy, Office of Science, Basic Energy Sciences (BES), Scientific User Facilities Division; (3) Eugene P. Wigner Fellowship at Oak Ridge National Laboratory; (4) Laboratory Directed Research and Development Program of Oak Ridge National Laboratory.

Notes

The authors declare no competing financial interest.

■ ACKNOWLEDGMENTS

Synthesis science including crystal growth, processing, optical characterization, TEM analysis, AFM studies (M.M.S., K.W., G.E., D.B.G., C.M.R., A.A.P., G.D., M.T., N.C.) was supported by the U.S. Department of Energy, Office of Science, Basic Energy Sciences (BES), Materials Sciences and Engineering Division and performed in part as a user project at the Center for Nanophase Materials Sciences, which is a DOE Office of Science User Facility. Characterization science at CNMS including lithography and device fabrication, electrical transport measurements, and theoretical calculations (K.X., M.W.L., A.O., B.G.S., A.B., M.Y.) were performed at the Center for Nanophase Materials Sciences, a US Department of Energy Office of Science User Facility. L.L. was supported by a Eugene P. Wigner Fellowship at the Oak Ridge National Laboratory. Y.S.K. was supported by the Laboratory Directed Research and Development Program of Oak Ridge National Laboratory, managed by UT-Battelle, LLC, for the U.S. DOE.

■ REFERENCES

- (1) Mas-Balleste, R.; Gomez-Navarro, C.; Gomez-Herrero, J.; Zamora, F. *Nanoscale* **2011**, *3*, 20–30.
- (2) Miro, P.; Ghorbani-Asl, M.; Heine, T. *Angew. Chem., Int. Ed.* **2014**, *53*, 3015–8.
- (3) Amani, M.; Lien, D. H.; Kiriya, D.; Xiao, J.; Azcatl, A.; Noh, J.; Madhupathy, S. R.; Addou, R.; Santosh, K. C.; Dubey, M.; Cho, K.; Wallace, R. M.; Lee, S. C.; He, J. H.; Ager, J. W.; Zhang, X.; Yablonovitch, E.; Javey, A. *Science* **2015**, *350*, 1065–1068.
- (4) Bhimanapati, G. R.; Lin, Z.; Meunier, V.; Jung, Y.; Cha, J.; Das, S.; Xiao, D.; Son, Y.; Strano, M. S.; Cooper, V. R.; Liang, L. B.; Louie, S. G.; Ringe, E.; Zhou, W.; Kim, S. S.; Naik, R. R.; Sumpter, B. G.; Terrones, H.; Xia, F. N.; Wang, Y. L.; Zhu, J.; Akinwande, D.; Alem, N.; Schuller, J. A.; Schaak, R. E.; Terrones, M.; Robinson, J. A. *ACS Nano* **2015**, *9*, 11509–11539.
- (5) Rezk, A. R.; Carey, B.; Crimes, A. F.; Lau, D. W. M.; Gibson, B. C.; Zheng, C. X.; Fuhrer, M. S.; Yeo, L. Y.; Kalantar-zadeh, K. *Nano Lett.* **2016**, *16*, 849–855.
- (6) Lin, J. H.; Pantelides, S. T.; Zhou, W. *ACS Nano* **2015**, *9*, 5189–5197.
- (7) Azizi, A.; Zou, X.; Ercius, P.; Zhang, Z.; Elías, A. L.; Perea-López, N.; Stone, G.; Terrones, M.; Yakobson, B. I.; Alem, N. *Nat. Commun.* **2014**, *5*, 4867.
- (8) Zhang, K.; Feng, S.; Wang, J.; Azcatl, A.; Lu, N.; Addou, R.; Wang, N.; Zhou, C.; Lerach, J.; Bojan, V.; Kim, M. J.; Chen, L.-Q.; Wallace, R. M.; Terrones, M.; Zhu, J.; Robinson, J. A. *Nano Lett.* **2015**, *15*, 6586–6591.
- (9) Gong, Y.; Liu, Z.; Lupini, A. R.; Shi, G.; Lin, J.; Najmaei, S.; Lin, Z.; Elías, A. L.; Berkdemir, A.; You, Ge.; Terrones, H.; Terrones, M.; Vajtai, R.; Pantelides, S. T.; Pencycook, S. J.; Lou, J.; Zhou, W.; Ajayan, P. M. *Nano Lett.* **2014**, *14*, 442–449.
- (10) Ago, H.; Fukamachi, S.; Endo, H.; Solís-Fernández, P.; Mohamad Yunus, R.; Uchida, Y.; Panchal, V.; Kazakova, O.; Tsuji, M. *ACS Nano* **2016**, *10*, 3233–3240.
- (11) Wang, X.; Xia, F. *Nat. Mater.* **2015**, *14*, 264–265.
- (12) Robinson, B. J.; Giusca, C. E.; Gonzalez, Y. T.; Kay, N. D.; Kazakova, O.; Kolosov, O. V. *2D Mater.* **2015**, *2* (1), 015005.
- (13) Ataca, C.; Ciraci, S. *J. Phys. Chem. C* **2011**, *115*, 13303–13311.
- (14) Choi, J.; Zhang, H.; Choi, J. H. *ACS Nano* **2016**, *10*, 1671–1680.
- (15) Lin, Z.; Carvalho, B. R.; Kahn, E.; Lv, R.; Rao, R.; Terrones, H.; Pimenta, M. A.; Terrones, M. *2D Mater.* **2016**, *3*, 022002.
- (16) Lehtinen, O.; Komsa, H. P.; Pulkin, A.; Whitwick, M. B.; Chen, M. W.; Lehnert, T.; Mohn, M. J.; Yazyev, O. V.; Kis, A.; Kaiser, U.; Krasheninnikov, A. V. *ACS Nano* **2015**, *9*, 3274–3283.

- (17) Liu, H. J.; Zheng, H.; Yang, F.; Jiao, L.; Chen, J. L.; Ho, W. K.; Gao, C. L.; Jia, J. F.; Xie, M. H. *ACS Nano* **2015**, *9*, 6619–6625.
- (18) Li, H.; Tsai, C.; Koh, A. L.; Cai, L.; Contryman, A. W.; Fragapane, A. H.; Zhao, J.; Han, H. S.; Manoharan, H. C.; Abild-Pedersen, F.; Nørskov, J. K.; Zheng, X. *Nat. Mater.* **2015**, *15*, 4564.
- (19) Zan, R.; Ramasse, Q. M.; Jalil, R.; Georgiou, T.; Bangert, U.; Novoselov, K. S. *ACS Nano* **2013**, *7*, 10167–10174.
- (20) Liu, Y. L.; Nan, H. Y.; Wu, X.; Pan, W.; Wang, W. H.; Bai, J.; Zhao, W. W.; Sun, L. T.; Wang, X. R.; Ni, Z. H. *ACS Nano* **2013**, *7*, 4202–4209.
- (21) Komsa, H. P.; Kurasch, S.; Lehtinen, O.; Kaiser, U.; Krasheninnikov, A. V. *Phys. Rev. B: Condens. Matter Mater. Phys.* **2013**, *88*, 035301.
- (22) Kang, N. R.; Paudel, H. P.; Leuenberger, M. N.; Tetard, L.; Khondaker, S. I. *J. Phys. Chem. C* **2014**, *118*, 21258–21263.
- (23) Enyashin, A. N.; Bar-Sadan, M.; Houben, L.; Seifert, G. *J. Phys. Chem. C* **2013**, *117*, 10842–10848.
- (24) Gutierrez, H. R.; Perea-Lopez, N.; Elias, A. L.; Berkdemir, A.; Wang, B.; Lv, R.; Lopez-Urias, F.; Crespi, V. H.; Terrones, H.; Terrones, M. *Nano Lett.* **2013**, *13*, 3447–3454.
- (25) Hong, J. H.; Hu, Z. X.; Probert, M.; Li, K.; Lv, D. H.; Yang, X. N.; Gu, L.; Mao, N. N.; Feng, Q. L.; Xie, L. M.; Zhang, J.; Wu, D. Z.; Zhang, Z. Y.; Jin, C. H.; Ji, W.; Zhang, X. X.; Yuan, J.; Zhang, Z. *Nat. Commun.* **2015**, *6*, 7293.
- (26) Mahjouri-Samani, M.; Tian, M.; Wang, K.; Boulesbaa, A.; Rouleau, C. M.; Puzos, A. A.; McGuire, M. A.; Srijanto, B. R.; Xiao, K.; Eres, G.; Duscher, G.; Geohegan, D. B. *ACS Nano* **2014**, *8*, 11567–11575.
- (27) Terrones, H.; Del Corro, E.; Feng, S.; Poumirol, J. M.; Rhodes, D.; Smirnov, D.; Pradhan, N. R.; Lin, Z.; Nguyen, M. A. T.; Elias, A. L.; Mallouk, T. E.; Balicas, L.; Pimenta, M. A.; Terrones, M. *Sci. Rep.* **2014**, *4*, 4215.
- (28) Tonndorf, P.; Schmidt, R.; Bottger, P.; Zhang, X.; Borner, J.; Liebig, A.; Albrecht, M.; Kloc, C.; Gordan, O.; Zahn, D. R. T.; de Vasconcelos, S. M.; Bratschkitsch, R. *Opt. Express* **2013**, *21*, 4908–4916.
- (29) Lee, C.; Yan, H.; Brus, L. E.; Heinz, T. F.; Hone, J.; Ryu, S. *ACS Nano* **2010**, *4*, 2695–2700.
- (30) Shaw, J. C.; Zhou, H. L.; Chen, Y.; Weiss, N. O.; Liu, Y.; Huang, Y.; Duan, X. F. *Nano Res.* **2014**, *7*, 511–517.
- (31) Ross, J. S.; Wu, S. F.; Yu, H. Y.; Ghimire, N. J.; Jones, A. M.; Aivazian, G.; Yan, J. Q.; Mandrus, D. G.; Xiao, D.; Yao, W.; Xu, X. D. *Nat. Commun.* **2013**, *4*, 2498.
- (32) Tongay, S.; Zhou, J.; Ataca, C.; Liu, J.; Kang, J. S.; Matthews, T. S.; You, L.; Li, J. B.; Grossman, J. C.; Wu, J. Q. *Nano Lett.* **2013**, *13*, 2831–2836.
- (33) Krivanek, O. L.; Chisholm, M. F.; Nicolosi, V.; Pennycook, T. J.; Corbin, G. J.; Dellby, N.; Murfitt, M. F.; Own, C. S.; Szilagyi, Z. S.; Oxley, M. P.; Pantelides, S. T.; Pennycook, S. J. *Nature* **2010**, *464*, 571–574.
- (34) Pennycook, S. J. *Ultramicroscopy* **2012**, *123*, 28–37.
- (35) Mahjouri-Samani, M.; Lin, M. W.; Wang, K.; Lupini, A. R.; Lee, J.; Basile, L.; Boulesbaa, A.; Rouleau, C. M.; Puzos, A. A.; Ivanov, I. N.; Xiao, K.; Yoon, M.; Geohegan, D. B. *Nat. Commun.* **2015**, *6*, 8749.
- (36) Liang, L. B.; Meunier, V. *Nanoscale* **2014**, *6*, 5394–5401.
- (37) Mignuzzi, S.; Pollard, A. J.; Bonini, N.; Brennan, B.; Gilmore, I. S.; Pimenta, M. A.; Richards, D.; Roy, D. *Phys. Rev. B: Condens. Matter Mater. Phys.* **2015**, *91*, 195411.
- (38) Ferrari, A. C.; Basko, D. M. *Nat. Nanotechnol.* **2013**, *8*, 235–246.
- (39) del Corro, E.; Terrones, H.; Elias, A.; Fantini, C.; Feng, S.; Nguyen, M. A.; Mallouk, T. E.; Terrones, M.; Pimenta, M. A. *ACS Nano* **2014**, *8*, 9629–9635.
- (40) Frey, G. L.; Tenne, R.; Matthews, M. J.; Dresselhaus, M. S.; Dresselhaus, G. *Phys. Rev. B: Condens. Matter Mater. Phys.* **1999**, *60*, 2883–2892.
- (41) Pradhan, N. R.; Rhodes, D.; Xin, Y.; Memaran, S.; Bhaskaran, L.; Siddiq, M.; Hill, S.; Ajayan, P. M.; Balicas, L. *ACS Nano* **2014**, *8*, 7923–7929.
- (42) Wang, X.; Gong, Y.; Shi, G.; Chow, W. L.; Keyshar, K.; Ye, G.; Vajtai, R.; Lou, J.; Liu, Z.; Ringe, E.; Tay, B. K.; Ajayan, P. M. *ACS Nano* **2014**, *8*, 5125–31.
- (43) Son, N. T.; Kim, Y.-S.; Janzén, E. *Phys. Status Solidi RRL* **2015**, *9*, 707–710.
- (44) Gong, C.; Colombo, L.; Wallace, R. M.; Cho, K. *Nano Lett.* **2014**, *14*, 1714–20.
- (45) Kresse, G.; Furthmüller, J. *Phys. Rev. B: Condens. Matter Mater. Phys.* **1996**, *54*, 11169–11186.
- (46) Blochl, P. E. *Phys. Rev. B: Condens. Matter Mater. Phys.* **1994**, *50*, 17953–17979.
- (47) Togo, A.; Tanaka, I. *Scr. Mater.* **2015**, *108*, 1–5.